Geophysical Journal International

Geophys. J. Int. (2022) **231,** 584–596 https://doi.org/10.1093/gji/ggac206
Advance Access publication 2022 June 2
GJI General Geophysical Methods

Three-dimensional time-lapse inversion of transient electromagnetic data, with application at an Icelandic geothermal site

Longying Xiao [1,2] Gianluca Fiandaca [3] Pradip K. Maurya [1] Anders Vest Christiansen[1] and Léa Lévy[1,4,5]

[1] *HydroGeophysics Group, Department of Geoscience, Aarhus University,* 800*, Denmark E-mail:* *longying.xiao@gtk.fi*
[2] *Geological Survey of Finland (GTK), Vuorimiehentie* 5*,* 02151 *Espoo, Finland*
[3] *Department of Earth Sciences "Ardito Desio", University of Milano,* 20133*, Italy*
[4] *ÍSOR, Iceland GeoSurvey, Grensásvegur* 9*,* 108 *Reykjavik,* 108 *, Iceland*
[5] *Engineering Geology, Lunds Tekniska Högskola, Lund University,* 221 00*, Sweden*

Accepted 2022 May 30. Received 2022 April 24; in original form 2021 November 15

SUMMARY

Transient electromagnetic (TEM) is an efficient non-invasive method to map electrical conductivity distribution in the subsurface. This paper presents an inversion scheme for 3-D TEM time-lapse (TL) data using a generalized minimum support (MS) norm and its application to monitoring conductivity changes over time. In particular, two challenges for TL TEM applications are addressed: (i) the survey repetition with slightly different acquisition position, that is, because systems are not installed and (ii) non-optimal data coverage above the TL anomalies, for instance, due to the presence of infrastructure that limits the acquisition layout because of coupling. To address these issues, we developed a new TEM TL inversion scheme with the following features: (1) a multimesh approach for model definition and forward computations, which allows for seamless integration of data sets with different acquisition layouts; (2) 3-D sensitivity calculation during the inversion, which allows retrieving conductivity changes in-between TEM soundings and (3) simultaneous inversion of two data sets at once, imposing TL constraints defined in terms of a generalized MS norm, which ensures compact TL changes. We assess the relevance of our implementations through a synthetic example and a field example. In the synthetic example, we study the capability of the inversion scheme to retrieve compact time-lapse changes despite slight changes in the acquisition layout and the effect of data coverage on the retrieval of TL changes. Results from the synthetic tests are used for interpreting field data, which consists of two TEM data sets collected in 2019 and 2020 at the Nesjavellir high-temperature geothermal site (Iceland) within a monitoring project of H_2S sequestration. Furthermore, the field example illustrates the effect of the trade-off between data misfit and TL constraints in the inversion objective function, using the tuning settings of the generalized MS norm. Based on the results from both the synthetic and field cases, we show that our implementation of 3-D TL inversion has a robust performance for TEM monitoring.

Key words: Hydrogeophysics; Controlled source electromagnetics (CSEM); Inverse theory; Time-lapse inversion; Time-domain electromagnetic.

INTRODUCTION

Time-lapse (TL) inversion of resistivity has been used for inferring temporal changes in the subsurface for different environmental and engineering problems such as groundwater mapping (Doetsch *et al.* 2012; Singha *et al.* 2015), seawater intrusion delineation (Falgàs *et al.* 2009; Ogilvy *et al.* 2009; Vann *et al.* 2020), soil moisture assessment (Blanchy *et al.* 2020; Farzamian *et al.* 2021), gas sequestration (Doetsch *et al.* 2015; Auken *et al.* 2014), geothermal system monitoring (Peacock *et al.* 2013; Hermans *et al.* 2015) and oil production (Orange *et al.* 2009; Shantsev *et al.* 2020).

TL strategies can be roughly divided into three categories: (i) difference inversion (LaBrecque and Yang 2001; Ajo-Franklin *et al.* 2007; Carbajal *et al.* 2012; Bretaudeau *et al.* 2021) and ratio inversion (Daily *et al.* 1992), which take the difference/ratio of the observed data as data input and invert for model differences, allowing an efficient suppression of the systematic noise and lowering of the computational dimensionality; (ii) cascaded inversion (Oldenborger *et al.* 2007; Miller *et al.* 2008; McLachlan *et al.* 2020), which inverts the data sets sequentially based on the previous inversion result and (iii) simultaneous inversion of two (or multiple) data sets with constrained models (Kim *et al.* 2009; Hayley *et al.* 2011).

Results of difference/ratio and cascaded inversions are highly influenced by the reference model, and inversion artefacts can easily propagate through subsequent inversions. Furthermore, difference/ratio inversion requires a rigorously matching acquisition setup, which is not always achievable due to budget reasons (instrument cost) or the risk of instrument damage by weather and animals. On the contrary, simultaneous inversion treats all time steps in the inversion equivalently, so it is less prone to artefact propagation from one model to another, and the instrument setup may vary among acquisitions. Furthermore, in iterative inversion schemes, it allows the models of the time steps to 'communicate' after each iteration and avoids models being updated in significantly different inversion paths. However, the computational expense is multiplied since the size of data space and model space are proportional to the number of TL steps.

TL inversion strategies differ significantly also because of the different regularization schemes applicable to the TL constraints. In this regard, Carbajal *et al.* (2012) compared the performance of the classic L2 norm for TL constraints, which penalizes the squares of parameter variations between TL steps, to the minimum support (MS) norm (Portniaguine and Zhdanov, 1999, Zhdanov *et al.* 2006b), which penalizes the number of inversion cells that vary, regardless of the magnitude of parameter variations. However, MS norms are usually challenging to tune, which led Fiandaca *et al.* (2015) to develop two generalizations of the MS norm for TL inversion, the symmetric and asymmetric generalized MS norms, which give good performance in focusing TL changes with easy-to-tune norm settings.

TL inversion, with different inversion strategies and regularizations, has been actively studied and applied in the field of electrical resistivity tomography (ERT) for more than two decades (LaBrecque and Yang 2001; Kim *et al.* 2009; Karaoulis *et al.* 2014; Lesparre *et al.* 2017; McLachlan *et al.* 2017; Bièvre *et al.* 2021). In addition, similar approaches have been gradually applied in inductive methods such as magnetotelluric (Carbajal *et al.* 2012; Rosas-Carbajal *et al.* 2015) and controlled source electromagnetic method (Shantsev *et al.* 2020; Bretaudeau *et al.* 2021; Hoversten and Schwarzbach 2021), which show superior sensitivity to conductive structures.

Nonetheless, to the best of our knowledge, TL inversion has never been applied to transient electromagnetic (TEM) data, even though the TEM method is widely used in near-surface resistivity distribution mapping (e.g. Auken *et al.* 2017). This is probably due to the specific challenges associated with TEM TL inversions: (i) data collection with consistent acquisition layouts (geometries, locations, etc.) is complicated with a moving measurement such as in airborne EM, but also with ground-based EM where the exact geometry and location of the transmitter loop can be cumbersome to reproduce identically without leaving the setup at the site; (ii) TEM surveys may result in different data density due to the unexpected coupling to infrastructure in different TL acquisition steps, or limitations in accessibility and (iii) 3-D TEM inversion, best suited for retrieving localized TL changes, requires intensive computational capacity in terms of both time consumption and memory cost.

We address these issues with the development of a new TEM TL inversion scheme in which: (i) forward and Jacobian computations are carried out in 3-D through the octree-based finite-element (FE) method (Xiao *et al.* 2022); (ii) the multimesh approach (Zhang *et al.* 2021) is used to decouple the forward/Jacobian mesh and inversion mesh so that the same inversion mesh can be used at different TL steps despite possible variations in acquisition layouts; (iii) the calculation burden in the modelling process is effectively alleviated owing to the domain decomposition strategy (Yang *et al.* 2013), which uses a local mesh for individual soundings and (iv) data sets acquired at different TL steps are inverted simultaneously, using the asymmetric generalized MS norm for TL constraints (Fiandaca *et al.* 2015), to obtain compact TL changes, that is, the smallest model variations compatible with the data.

The following sections of the paper are organized as follows: the principle of the TEM forward and inverse problems are described, together with the asymmetric MS norm. Then, we present a synthetic model, designed with complexity equivalent to the field case, to illustrate the relevance of our implementation compared to an independent inversion. This section also discusses the impact of data density on both independent and TL inversion performance. The following section describes the application of the new inversion algorithm to a field example. The field example consists of two TEM data sets collected with a one-year interval; the purpose of the surveys was to build a baseline model before a monitoring experiment of H_2S sequestration at the Nesjavellir geothermal power plant in Iceland. This sequestration experiment is part of the GEMGAS (Geo-Electrical Monitoring of H_2S Gas Sequestration) project (Lévy *et al.* 2020).

THEORY

Forward response

The time-domain forward problem is formulated as a boundary-value problem, deriving from Maxwell's equations:

$$\nabla \times \mathbf{e}(\mathbf{r}, t) = -\mu_0 \frac{\partial \mathbf{h}(\mathbf{r}, t)}{\partial t} \tag{1}$$

and

$$\nabla \times \mathbf{h}(\mathbf{r}, t) - \frac{\partial \mathbf{D}(\mathbf{r}, t)}{\partial t} = \mathbf{j}(\mathbf{r}, t) + \mathbf{j}_s(t). \tag{2}$$

where the electric field $\mathbf{e}(\mathbf{r}, t)$, magnetic field intensity $\mathbf{h}(\mathbf{r}, t)$, the dielectric displacement $\mathbf{D}(\mathbf{r}, t)$, and the current density $\mathbf{j}(\mathbf{r}, t)$ are functions of space, $\mathbf{r}(\mathbf{r} \in \Omega)$, and time, $t \in (0, T)$, μ_0 is the magnetic permeability of free space and $\mathbf{j}_s$ denotes the current source.

With the quasi-static approximation (displacement currents $\frac{\partial \mathbf{D}}{\partial t} = 0$), the use of Ohm's law for current density ($\mathbf{j} = \sigma \mathbf{E}$, where σ represents the electric conductivity), and the assumption that the media is isotropic and non-magnetizable and that electrical properties are independent on time (so induced polarization is neglected), the electrical field $\mathbf{e}(\mathbf{r}, t)$ obeys a diffusion equation:

$$\nabla \times \nabla \times \mathbf{e}(\mathbf{r}, t) + \mu_0 \sigma(\mathbf{r}) \frac{\partial \mathbf{e}(\mathbf{r}, t)}{\partial t} = -\frac{\partial \mathbf{j}_s(t)}{\partial t} \tag{3}$$

We solve eq. (3) following the method proposed by Xiao et al. (2022), where the equation is discretized in the time domain using the second-order backward Euler method (Butcher and Goodwin, 2008) and in the space domain using the FE method (Jin 2015).

Furthermore, the multimesh approach introduced by Zhang *et al.* (2021) is applied for decoupling the forward/Jacobian meshes and inversion mesh (Fig. 1). Individual meshes are used for each sounding as local meshes for forward/Jacobian calculations (octree meshes in this study, while tetrahedral meshes are used in Zhang

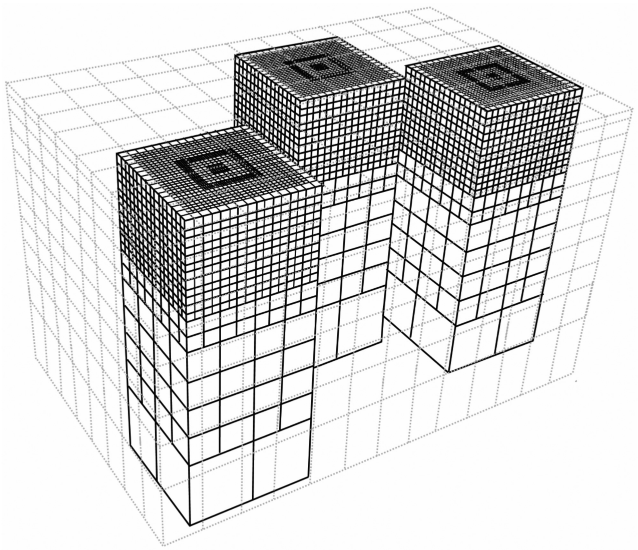

Figure 1. Multimesh approach illustration: local octree mesh (black) is used for forward response and Jacobian calculation at each sounding, and structured mesh (grey) is used for inversion model update.

et al. 2021), while a full-scale regular mesh that covers all the soundings is used as the inversion mesh. The model nodes in the regular inversion mesh are defined on the mesh nodes with uniform node spacing in the horizontal direction and log-increasing node spacing in the vertical direction (Christensen *et al.* 2017). The resistivity values in the cells of the forward meshes are obtained from the values of the inversion mesh through interpolation with an inverse distance weighting method (Madsen *et al.* 2020). The log-increasing node spacing in the vertical direction helps balance the sensitivity of deep and shallow areas of the model to avoid favouring shallow TL changes, as would happen with linear vertical node spacing.

The advantage of this method is threefold for TL TEM inversions. First, the computational complexity is minimized while the forward accuracy is maintained, owing to the domain decomposition. Secondly, it eases the process of enforcing spatial constraints for the inversion or incorporating prior knowledge, thanks to the regularity of the inversion mesh. Lastly, it overcomes the challenge of data repetition with matching layouts, providing the flexibility that surveys at different TL steps can be carried out at different locations within the research area.

Inversion

In the TL inversion scheme adopted in this study, two data sets $\mathbf{d}_1$ and $\mathbf{d}_2$ are inverted simultaneously to obtain the corresponding models $\mathbf{m}_1$ and $\mathbf{m}_2$ by constraining the model difference $\delta\mathbf{m} = \mathbf{m}_2 - \mathbf{m}_1$ (while $\mathbf{d}_1$ and $\mathbf{d}_2$ may differ in size, $\mathbf{m}_1$ and $\mathbf{m}_2$ are defined on identical meshes and have the same size, such that the difference in model parameters can be determined). Furthermore, in addition to the roughness constraint on individual models $\mathbf{m}_1$ and $\mathbf{m}_2$, roughness constraints are also applied to the model difference $\delta\mathbf{m}$. Defining the whole inversion data and model vectors $\mathbf{d}$ and $\mathbf{m}$ in terms of the concatenation of individual vectors as $\mathbf{d} = \begin{bmatrix}\mathbf{d}_1\\ \mathbf{d}_2\end{bmatrix}$ and $\mathbf{m} = \begin{bmatrix}\mathbf{m}_1\\ \mathbf{m}_2\end{bmatrix}$. The objective function Φ in our TL inversion scheme consists of four terms:

$$\Phi = \Phi_d(\delta\mathbf{d}) + \Phi_{TL}(\delta\mathbf{m}) + \Phi_{Rm}(\mathbf{r}) + \Phi_{Ru}(\delta\mathbf{r}) \tag{4}$$

where:

(1) Φ_d, Φ_{TL}, Φ_{Rm} and Φ_{Ru} represent the measures of the data difference, model update, roughness of model and roughness of model update, respectively. The last three terms represent the model regularizations of the inversion (Φ_{TL}, Φ_{Rm}, Φ_{Ru}): in particular, the TL term Φ_{TL} measures and minimizes the distance between $\mathbf{m}_1$ and $\mathbf{m}_2$, that is, the model update in the TL inversion; the model roughness term Φ_{Rm} minimizes the roughness of individual models and the measure Φ_{Ru} minimizes the roughness of the model updates.

(2) $\delta\mathbf{d} = \mathbf{d} - \mathbf{d}_{\mathrm{obs}}$ represents the difference between the forward response $\mathbf{d}$ and the observed data $\mathbf{d}_{\mathrm{obs}}$; $\delta\mathbf{m} = \mathbf{m}_2 - \mathbf{m}_1$ symbolizes the model update between two models, that is, model temporal variations; $\mathbf{r} = -\mathbf{R}_{\mathrm{m}}\mathbf{m}$ represents the model roughness through the roughness matrix $\mathbf{R}_{\mathrm{m}} = \begin{bmatrix}\mathbf{R}_{\mathrm{m}_1} & 0\\ 0 & \mathbf{R}_{\mathrm{m}_2}\end{bmatrix}$ and$\delta\mathbf{r} = -\mathbf{R}_{\mathrm{u}}\delta\mathbf{m}$ is the roughness of the model update.

The TL inversion is performed iteratively by following the practice established in AarhusInv (Auken *et al.* 2015). The approach is based on the Levenberg–Marquardt adaptive minimization scheme (Hanke 1997; Menke 2018), a weighted combination of the gradient descent method and the Gauss–Newton (GN) method. Norms different from L2 in eq. (4) are implemented through the iteratively reweighted least-squares (IRLS) approach following (Farquharson and Oldenburg 1998). The model vector $\mathbf{m}$ is updated at the $n+1$th iterative step:

$$\mathbf{m}_{n+1} = \mathbf{m}_n + \left[\mathbf{G}^{*T}_{(n)}\mathbf{C}^{*-1}_{(n)}\mathbf{G}^{*}_{(n)} + \lambda_{(n)}\mathbf{I}\right]^{-1} \cdot \left[\mathbf{G}^{*T}_{(n)}\mathbf{C}^{*-1}_{(n)}\delta\mathbf{d}^{*}_{(n)}\right] \tag{5}$$

Here, the damping parameter, $\lambda_{(n)}$, iteratively reweights the gradient descent approach and the GN method by scaling the identity matrix $\mathbf{I}$, $\mathbf{G}^*_{(n)}$ includes the Jacobian matrix of different partial derivatives, the vector update $\delta\mathbf{d}^*_{(n)}$ contains data, model roughness, and model difference; and $\mathbf{C}^{*-1}_{(n)}$ is the covariance matrix of data uncertainty and model roughness, as follows:

$$\mathbf{G}^*_{(n)} = \begin{bmatrix}\mathbf{G}_{(n)}\\ \mathbf{I}\\ \mathbf{R}_m\\ \mathbf{R}_u\end{bmatrix} \tag{6}$$

$$\delta\mathbf{d}^*_{(n)} = \begin{bmatrix}\delta\mathbf{d}_{(n)}\\ \delta\mathbf{m}_{(n)}\\ \mathbf{r}_{(n)}\\ \delta\mathbf{r}_{(n)}\end{bmatrix} = \begin{bmatrix}\mathbf{d}_{(n)} - \mathbf{d}_{obs}\\ \mathbf{m}_{2(n)} - \mathbf{m}_{1(n)}\\ -\mathbf{R}_m\mathbf{m}_{(n)}\\ -\mathbf{R}_u\delta\mathbf{m}_{(n)}\end{bmatrix} \tag{7}$$

$$\mathbf{C}^{*-1}_{(n)} = \begin{bmatrix}\mathbf{C}^{-1}_{\mathrm{obs}} & 0 & 0 & 0\\ 0 & \mathbf{W}'^{T-1}_{TL(n)}\mathbf{C}^{-1}_{TL}\mathbf{W}'_{TL(n)} & 0 & 0\\ 0 & 0 & \mathbf{W}'^{T-1}_{R_m(n)}\mathbf{C}^{-1}_{R_m}\mathbf{W}'_{R_m(n)} & 0\\ 0 & 0 & 0 & \mathbf{W}'^{T-1}_{R_u(n)}\mathbf{C}^{-1}_{R_u}\mathbf{W}'_{R_u(n)}\end{bmatrix} \tag{8}$$

In eq. (6), $\mathbf{G}_{(n)} = \begin{bmatrix}\mathbf{G}_{1(n)} & 0\\ 0 & \mathbf{G}_{2(n)}\end{bmatrix}$ represents the Jacobian of the two acquisitions, translated from the forward mesh to the inversion mesh following Madsen *et al.* (2020) and Zhang *et al.* (2021); $\mathbf{I}$ is the identity matrix and $\mathbf{R}_m$ and $\mathbf{R}_u$ are the roughness matrices on model and model update. In eq. (7), the data vector update $\delta\mathbf{d}^*_{(n)}$ includes the distance $\delta\mathbf{d}_{(n)}$between the nth forward response $\mathbf{d}_{(n)}$ and the observed data $\mathbf{d}_{\mathrm{obs}}$, the distance $\delta\mathbf{m}_{(n)}$ between the two models at the nth iteration, the roughness of the nth model vector $\mathbf{r}_{(n)} = -\mathbf{R}_m\mathbf{m}_{(n)}$ and the roughness of the model difference nth model vector $\delta\,\mathbf{r}_{(n)} = -\mathbf{R}_u\delta\mathbf{m}_{(n)}$. In eq. (8), the covariance matrix $\mathbf{C}^*$ is defined in terms of the covariance on the observed data $\mathbf{C}_{\mathrm{obs}}$, the TL covariance on the model difference $\mathbf{C}_{\mathrm{TL}}$ and the covariance on the roughness constraints $\mathbf{C}_{R_m}$ and $\mathbf{C}_{R_u}$. The elements of $\mathbf{C}_{\mathrm{obs}}$ indicates the noise level in the data, while the elements of $\mathbf{C}_{TL}$, $\mathbf{C}_{R_m}$ and $\mathbf{C}_{R_u}$ control the constraint strength from the model side. All four matrices are diagonal, thus, the data errors are assumed uncorrelated. In eq. (8), the matrices $\mathbf{W}'_{TL_{(n)}}$, $\mathbf{W}'_{R_m(n)}$ and $\mathbf{W}'_{R_u(n)}$ are the IRLS reweighting matrices that allows to define norms in the objective function different from the L2. In particular, for a given model vector $\mathbf{x}$ (equal to either $\delta\mathbf{m}$, $\mathbf{r}$ or $\delta\mathbf{r}$) and a given measure functional,

$$\Phi\ (\mathbf{x}) = \sum_{i=1}^{\mathrm{size}(\mathbf{X})} \varphi\,(x_i) \tag{9}$$

the matrices $\mathbf{W}'_{\eta}$ (where $\eta\ =\ TL$ or R_m or R_u) are linked to the measure Φ and the covariance matrices $\mathbf{C}_{\eta}$ following (Farquharson and Oldenburg 1998):

$$W'_{\eta_{i,i}} = \sqrt{\frac{\sqrt{C_{\eta_{i,i}}}}{2x_i}}\ \varphi'\,(x_i) \tag{10}$$

The stopping criterion of the iterative procedure in eq. (4) is implemented on the total misfit χ, defined as:

$$\chi\ =\left(\frac{\Phi_d\,(\delta\mathbf{d}) + \Phi_{TL}\,(\delta\mathbf{m}) + \Phi_{R_m}\,(\mathbf{r}) + \Phi_{R_u}\,(\delta\mathbf{r})}{N_d + N_{TL} + N_{R_m} + N_{R_u}}\right)^{\frac{1}{2}}$$
$$=\left(\frac{N_d\chi_d^2 + N_{TL}\chi_{TL}^2 + N_{R_m}\chi_{R_m}^2 + N_{R_u}\chi_{R_u}^2}{N_d + N_{TL} + N_{R_m} + N_{R_u}}\right)^{\frac{1}{2}} \tag{11}$$

In which:

(1) N_d, N_{TL}, N_{R_m}, N_{R_u} represent the number of data points, the number of TL constraints and the number of roughness constraints on model and model update.

(2) $\chi_d = \left(\frac{\delta\mathbf{d}^T\mathbf{C}_{\mathrm{obs}}^{-1}\delta\mathbf{d}}{N_d}\right)^{\frac{1}{2}}$ represents the data misfit.

(3) $\chi_{TL} = \left(\frac{\delta\mathbf{m}^T\mathbf{W}_{TL}^T\mathbf{C}_{TL}^{-1}\mathbf{W}_{TL}\delta\mathbf{m}}{N_{TL}}\right)^{\frac{1}{2}}$ represents the TL model penalty.

(4) $\chi_{R_m} = \left(\frac{\mathbf{r}^T\mathbf{W}_{R_m}^T\mathbf{C}_{R_m}^{-1}\mathbf{W}_{R_m}r}{N_{R_m}}\right)^{\frac{1}{2}}$ represents the roughness model penalty.

(5) $\chi_{Ru} = \left(\frac{\delta\mathbf{r}^T\mathbf{W}_{R_u}^T\mathbf{C}_{R_u}^{-1}\mathbf{W}_{R_u}\delta\mathbf{r}}{N_{R_u}}\right)^{\frac{1}{2}}$ represents the roughness model difference penalty.

The matrices $\mathbf{W}_{\eta}$ (where $\eta\ =\ TL$ or R_m or R_u) are linked to the measure Φ and the covariance matrices $\mathbf{C}_{\eta}$ as:

$$W_{\eta_{i,i}} = \sqrt{\frac{C_{\eta_{i,i}}}{x_i^2}}\ \varphi\,(x_i) \tag{12}$$

The inversion is carried out in logarithmic data and model spaces. The forward response $\mathbf{d}_{(n)}$ of eq. (3) and the Jacobian calculation $\mathbf{G}_{(n)}$ are computed for 3-D TEM data following the routine devised by Xiao *et al.* (2022). The inversion process is terminated when the variation of the total misfit between two consecutive iterations is smaller than a defined threshold (e.g. 1 per cent).

Asymmetric minimum support norm for time-lapse model difference

In this study, the measure of the model difference $\Phi_{TL}(\delta\mathbf{m})$ in the objective function of eq. (4) is defined in terms of an MS function instead of the classical L2 norm. While the L2 measure penalizes the sum of the squared difference of the components of the vector $\delta\mathbf{m}\ = \mathbf{m}_2\ - \mathbf{m}_1$, the MS functional penalizes the number of components $\delta\ \mathrm{m}_i = \mathrm{m}_{2,\mathrm{i}}\ - \mathrm{m}_{1,\mathrm{i}}$ that differ 'significantly' favour compact TL changes. Researchers have proposed different solutions for defining the significance of parameter differences in MS functionals for their applications (Last and Kubik 1983; Zhdanov and Tolstaya 2004; Zhdanov *et al.* 2006a; Ajo-Franklin *et al.* 2007; Kim and Cho 2011; Carbajal *et al.* 2012; Vignoli *et al.* 2012; Fiandaca *et al.* 2015). In particular, Fiandaca *et al.* (2015) proposed a definition of generalized asymmetric MS, which is an easy-to-tune regulation to find globally optimal compatibility between data and model variation. The analytical expression of the *i*th component of the functional in eq. (9) is expressed as:

$$\varphi_{MS}\ (x_i) = \alpha^{-1}\left[(1-\beta)\cdot\frac{\left(x_i^2/\sigma_i^2\right)^{p_1}}{\left(x_i^2/\sigma_i^2\right)^{p_1}+1} + \beta\cdot\frac{\left(x_i^2/\sigma_i^2\right)^{p_2}}{\left(x_i^2/\sigma_i^2\right)^{p_2}+1}\right] \tag{13}$$

$$\beta\ = \frac{\left(x_i^2/\sigma_i^2\right)^{\max(p_1,p_2)}}{\left(x_i^2/\sigma_i^2\right)^{\max(p_1,p_2)}+1} \tag{14}$$

where $x_i =\ \delta\mathrm{m}_i$ represents the difference of the *i*th component of the model difference and α, p_1, p_2 and σ_i represent the MS settings. The norm settings have the following meaning:

(1) The setting σ_i symbolizes the threshold value that defines the 'significance' of a parameter change because σ_i represents the transition point in the MS functional: $\delta\mathrm{m}_i \ll \sigma_i$ gives a zero penalty in the objective function, that is, $\varphi_{MS}\,(\delta\mathrm{m}_i) =\ 0$; $\delta\mathrm{m}_i \gg \sigma_i$ gives the maximum penalty $\varphi_{MS}\,(\delta\mathrm{m}_i) = \alpha^{-1}$; $\delta\ \mathrm{m}_i = \sigma_i$ represent the transition point at which half penalty $\varphi_{MS}\,(\delta\mathrm{m}_i) = 0.5\cdot\alpha^{-1}$ is reached. It is expressed typically as a fixed fraction (10 per cent–30 per cent) of the expected relative parameter (e.g. resistivity) variation, which can be estimated from either prior information of underlying temporal changes or a standard (e.g. L2) TL inversion.

(2) The setting α controls the maximum penalty, and hence the relative weight of data and model measures in the objective function affects the size of TL changes. $N_{\mathrm{transitions}}$ is defined as the expected number of model parameters that differ 'significantly' (i.e. above the transition point $\delta\ \mathrm{m}_i = \sigma_i$) in TL inversion. Fiandaca *et al.* (2015) suggest using α values bigger than $\alpha\ =\ \frac{N_{\mathrm{transitions}}}{N_{TL}}$, such that in eq. (11) $\chi_{TL}\ < 1$.

(3) The settings p_1 and p_2 control the shape of φ_{MS} before and after the transition point $\delta\ \mathrm{m}_i = \sigma_i$ (the sharpness of the transition increases with p), and determine how the focus depends on the other settings σ and α. Fiandaca *et al.* (2015) showed that $p_1 =\ 1.35$ and $p_2 =\ 2$ give the weakest overall dependance of the inversion results on the σ and α settings.

A complete study of the 3-D TEM TL effects on the four MS tuning settings is beyond the scope of this study, but it is worthy of future investigation. Instead, the novelty of this work relies not only on the use of the old MS TL regularization but also on the application of TEM data with 3-D modelling. For this reason, only the results with the optimal p_1 and p_2 suggested by Fiandaca et al. (2015) are presented (i.e. $p_1 =\ 1.35$ and $p_2 =\ 2$), and only one value for σ_i is used (i.e. a relative value of $\sigma_i =\ 0.1$), for both synthetic and field data. This σ_i value was chosen, as suggested by Fiandaca et al. (2015), by starting from a classic independent and smooth (L2) TL inversion of the field data, which shows resistivity variations above 10 per cent (the traditional L2 time-TL results are not shown in this work for brevity).

However, for both synthetic and field data, the inversion results are shown for various values of the setting α, which is the setting with the most considerable influence on TL results. This is because, contrary to Fiandaca *et al.* (2015), in this study, the number of TL constraints N_{TL} is much bigger than the number of data N_d ($N_{TL} \gg N_d$), and the risk of over-regularizing the inversion through the TL constraint is significant. Consequently, both synthetic and field data are analysed for different α values to explicitly study the dependence of inversion results on the balance between TL constraints and data misfit in the objective function.

NUMERICAL EXPERIMENTS

To investigate the transition resolution of the implementation and the dependence on data density given by the 3-D sensitivity, we designed two sets of synthetic examples: coarse and dense acquisition layouts, with *xy* sounding distances of 300 and 150 m, respectively. The resistive background media is an idealized two-layered model with a 1000 $\Omega \cdot$ m top layer (with a thickness of 50 m) underlain by a 100 $\Omega \cdot$ m homogeneous half-space, following the resistivity background values of the field case illustrated in the next section.

A 3-D conductive anomaly with a resistivity of 4 $\Omega \cdot$ m and a thickness of 50 m is embedded in the second layer. Its horizontal extent grows from 320 m x 300 m in the first measurement to 460 m x 300 m in the second measurement (black and grey dashed lines in Fig. 2) to simulate the TL changes. The 300 m sounding interval in the *x*- and *y*-directions of the coarse acquisition results in 16 soundings to cover the anomaly adequately. The dense acquisition halves the distance and requires 35 soundings, as shown in Fig. 2. In addition, since it is challenging to ensure soundings from different surveys meet the same positions, we simulate the soundings with slight *xy* displacements (black and grey solid lines in Fig. 2 indicate the TEM transmitter positions).

We modelled a central-loop WalkTEM system (Nyboe *et al.* 2010) with a 50×50 m^2 transmitter coil, convolving the impulse response with the waveform, bandwidth of the receiver coil and low pass filter of the electronics. Two system moments, with low moment gate centre times from 9.19×10^{-6} to 6.78×10^{-4} s and high moment gate centre times from 2.07×10^{-5} to 1.22×10^{-2} s, were simulated with different shapes of the transmitted waveforms, in order to obtain both shallow imaging and deep penetration (Auken *et al.* 2019). We used the 3-D FE solver from Xiao *et al.* (2022) to generate the forward response. The model space, using octree meshes, is refined locally close to the transmitter and receiver, where the electric fields change rapidly. The forward domain was decomposed with one local mesh for each transmitter–receiver system (Xiao *et al.* 2022). The input data were contaminated with 3 per cent of relative Gaussian noise for all time gates.

The stopping criterion for all inversions is based on the total misfit variation, the variation in the squared root of the objective function (eq. 11), which must be smaller than 1 per cent in our case. The same starting model was used for all inversions, a homogeneous 100 Ω m half-space. We conducted inversions for each acquisition layout: two independent inversions (i.e. Models 1 and 2) and TL inversions, varying the α MS tuning setting (eq. 13), that is, the weight of the TL constraints in the objective function. The number of iterations and the final data misfit of the inversion jobs are listed in Table 1 (the TL results are listed only for $\alpha = 3$). The inversions converged with similar data misfits and iteration numbers.

Inversion results are shown along a W-E section at the middle of the models (as shown by the red in Fig. 2). Figs 3 and 4 show the inversion results with $\alpha = 3$ along the section for the coarse and dense acquisition layouts, respectively: the true resistivity distribution of the two model sections (a and d), the corresponding independent inversions (b and e) and TL inversion sections (c and f); the third figure columns (g–i) are the resistivity ratios of the two model parameter vectors ($\mathbf{m}_2/\ \mathbf{m}_1$) at the section. The dotted white lines symbolize the anomaly position. Fig. 5 shows the TL inversion results for three different α-values (3, 30 and 300) for both coarse and dense layouts.

The inversion results in Fig. 3, that is, with the coarse acquisition layout, show that the conductive body grows more extensive over time. Still, it is hard to delineate the shape of the anomaly, especially for Model 1. This behaviour is better evidenced in the resistivity ratio sections: both independent and TL inversion reveal the increasing conductive body in the right-hand part of the anomaly but have difficulty resolving the changes in the left-hand region. In addition, the connecting conductive (blue) changes in between are artefacts. The missing resolution in the left-hand region is mainly caused by the poor data coverage compared to the size of the anomaly in Model 1, in which the conductive anomaly has no complete coverage by the soundings. However, the TL inversion retrieves a more focused TL image with fewer inversion artefacts.

The resolution of the model anomaly improves significantly when we halve the sounding distance. In Fig. 4, the two models are recovered to a satisfactory level in both the independent inversions and the TL inversion. However, the resistivity ratio highlights the lower quality of the independent inversions. Together with the two conductive blocky changes (blue), a resistivity increase and decrease are present all around the section. The ratio image of the TL inversion has much clearer background, and the anomaly boundary is sharper.

Fig. 5 shows the TL inversion results as a function of α: the resistivity ratios of the TL inversions present no resistivity overestimation (red areas) with $\alpha = 3$. At the same time, artefacts outside the anomaly outlines appear for higher values ($\alpha = 30$ and 300). The missing resolution in the left-hand region of the coarse layout diminishes with $\alpha > 3$, but almost no distinction appears between the true anomalies and the connecting conductive (blue) changes in between. The TL results with dense coverage maintain the capability of resolving the true conductive anomalies regardless of the α value, but resistive artefacts grow with α.

Overall, the 3-D sensitivity of the TEM measurements allows us to retrieve TL changes with an acquisition layout that does not entirely cover the conductive anomaly. However, significantly better results are achieved with increased data coverage. Furthermore, the focusing scheme significantly improves the retrieval of TL changes, with sharper anomaly boundaries and a more homogenous background. With coarse coverage, the capability of resolving the true TL differences is more affected by the value of the MS tuning setting α.

FIELD EXAMPLE

Geothermal gas re-injection is becoming a critical step in mitigating air pollution caused by geothermal exploitation. Re-injected acid gases (mostly CO_2 and H_2S) are expected to mineralize, but monitoring such mineralization processes in the subsurface is challenging. The GEMGAS project aims to test the capability of several geophysical methods, including TEM, to monitor the sequestration of a small-scale H_2S injection at the Nesjavellir power plant in Southwest Iceland (Lévy *et al.* 2020). H_2S injection is expected to trigger basaltic glass dissolution, resulting in the precipitation of

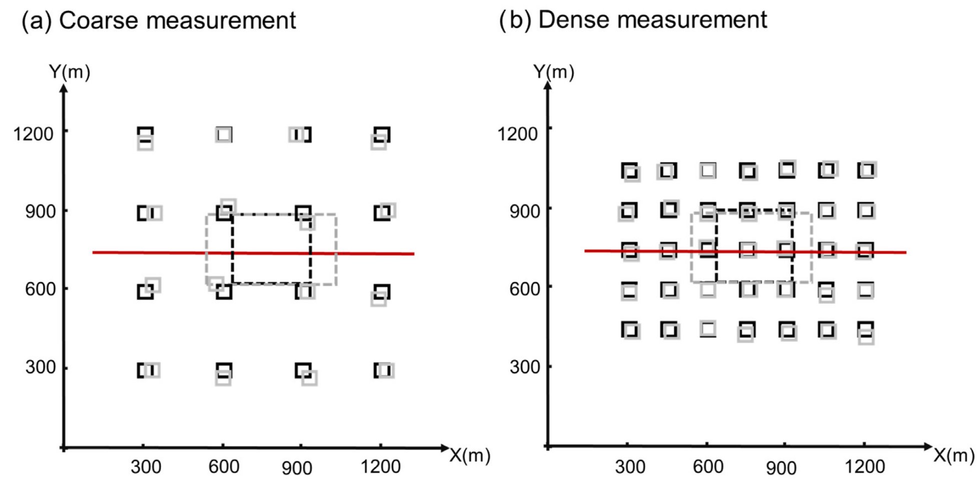

Figure 2. Coarse and dense acquisition layouts. The black rectangles represent the layout in the first measurement, and the grey ones represent the second measurement. The dashed lines symbolize the top view of the 3-D anomaly in the first (black) and second (grey) measurement. The red lines represent the position of the profile along which the inversion results are shown.

Table 1. The number of iterations/data misfits of the independent (Ind-) and time-lapse (TL-) inversions with coarse and dense measurement layout.

Layout / Inversion	Ind-Model 1	Ind-Model 2	TL-Total	TL-Model 1	TL-Model2
Coarse	10 / 1.01	10 / 1.00	10 / 1.26	– / 1.24	– / 1.27
Dense	12 / 1.04	11 / 1.20	9 / 1.26	– / 1.18	– / 1.33

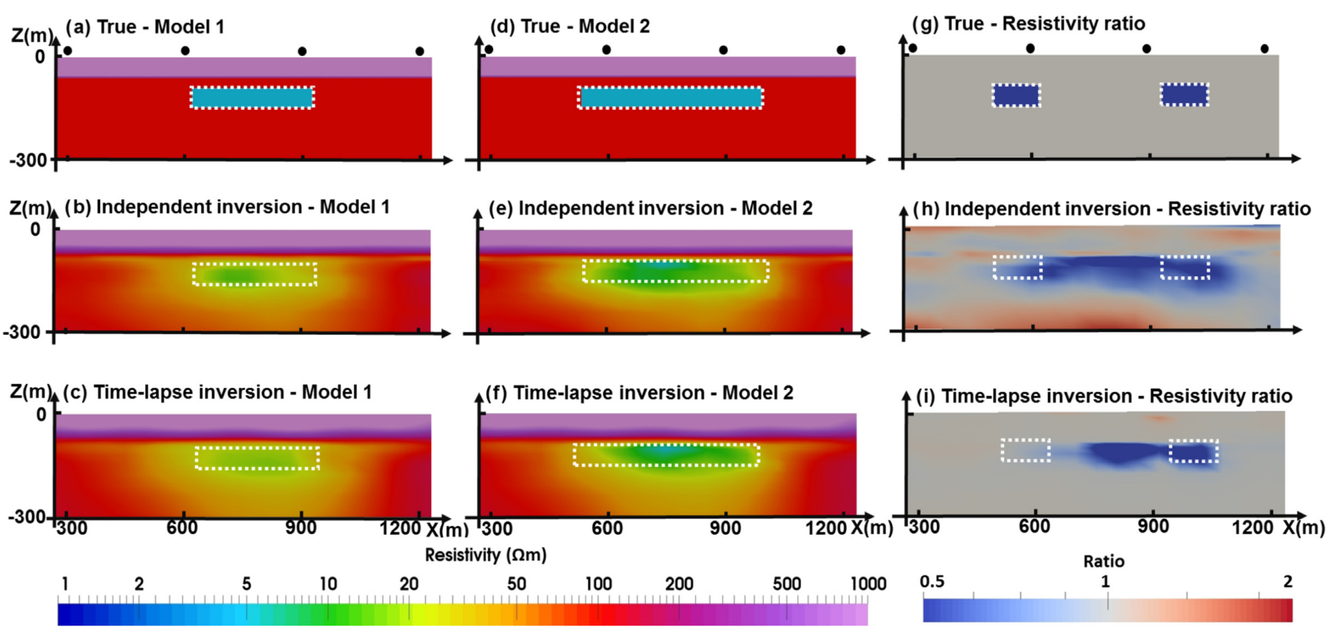

Figure 3. Model sections and resistivity ratios of independent and TL inversion results using the coarse acquisition layout. Black dots on the top sections represent the sounding positions. White dashed lines represent the outlines of the true conductive anomalies.

pyrite and clay minerals, which should be reflected by changes in the electrical properties of the subsurface (Lévy *et al.* 2018, 2019, Prikryl *et al.* 2018). Before the H_2S injection in 2021 January, two sets of TEM and ERT data were collected in 2019 and 2020 to obtain a baseline model and evaluate the resistivity variability at the site (either natural or caused by power plant operations). TL inversion of these baseline data sets is the focus of this section, while post-injection monitoring are not addressed further in this paper.

The ground-based TEM data acquisition used the WalkTEM system, with a 50 × 50 m^2 transmitter coil. Data were acquired with two magnetic dipole moments, with low moment gate center times from 9.19×10^{-6} to 6.78×10^{-4} s and high moment gate centre times from 2.07×10^{-5} to 1.22×10^{-2} s. The same starting model, homogeneous 100 Ω·m half-space, and stopping criterion, the total misfit variation smaller than 1 per cent, are used for all inversions. The same spatial constraints are applied to both TL and independent inversions.

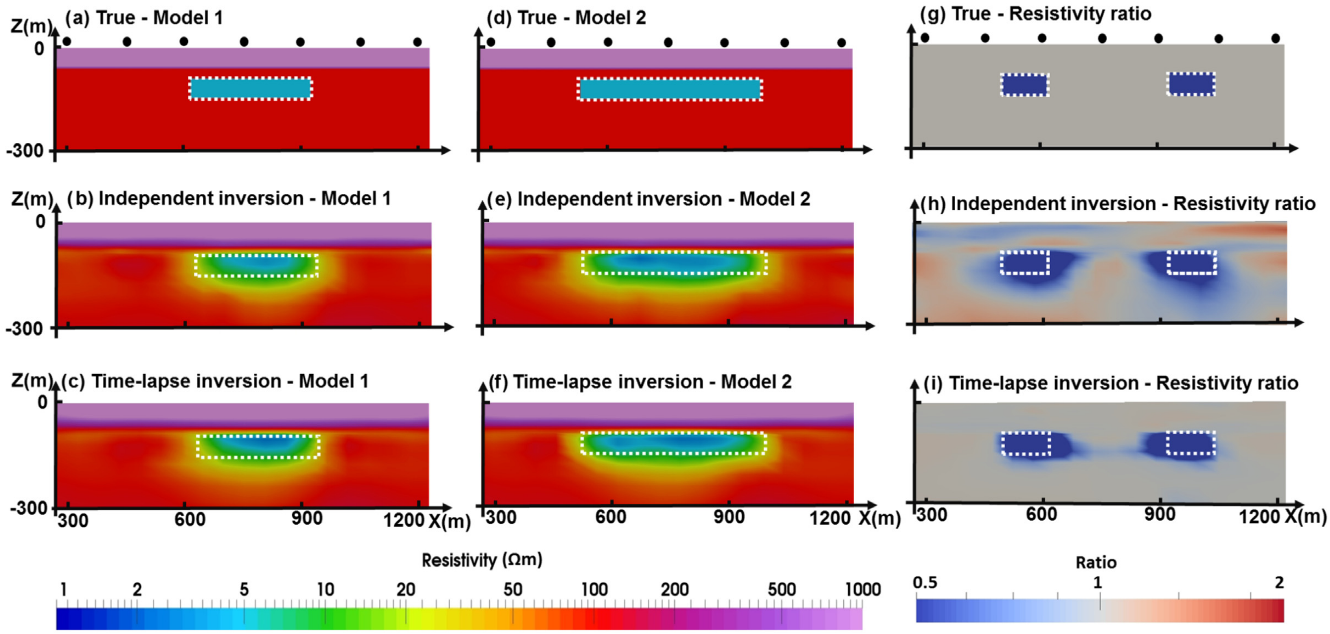

Figure 4. Model sections and resistivity ratios of independent and TL inversion results using the dense acquisition layout. Black dots on the top sections represent the sounding positions. White dashed lines represent the outlines of the true conductive anomalies.

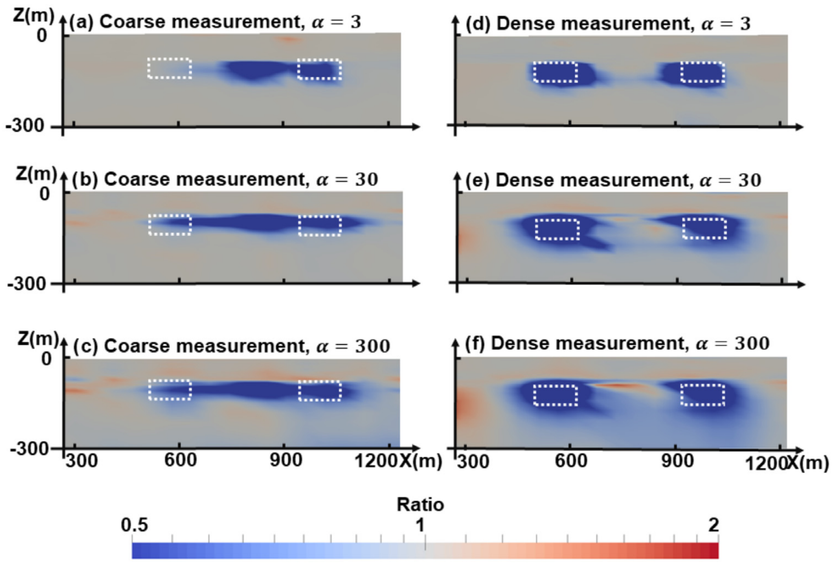

Figure 5. Resistivity ratios of TL inversion results using different values for the MS setting α (eq. 13): top row $\alpha = 3$; middle row $\alpha = 30$; bottom row $\alpha = 300$; left-hand column, coarse acquisition layout and right-hand column, dense acquisition layout. White dashed lines represent the outlines of the true conductive anomalies.

Fig. 6 shows the acquisition layout, with 20 soundings acquired in 2019 and 15 soundings in 2020, with no data coverage in the vicinity of the power plant infrastructure (yellow lines). The different number of soundings is due to the additional inductive coupling evidenced in the 2020 TEM data, with more soundings completely removed during data processing in 2020. The coupling was caused not only by the power plant infrastructure but also by metal fences present in the area and not shown on the map. Unfortunately, the area affected by coupling is also where H_2S injection is taking place. In the following, the inversion models will be shown in 3-D view and along with two profiles, shown in Fig. 6: the profile indicated by the red line, running close to the TEM soundings; the profile indicated by the dashed black line, along which ERT data have been acquired in 2020 (with an electrode distance of 10 m).

This latter profile is shown in Fig. 7, compared to the ERT results. A similar resistivity pattern appears in both inversions, with a strong conductive anomaly around $x = 1000$ m along the profile, in the vicinity of one of the injection well at Nesjavellir power plant (Lévy *et al.* 2020), where hot water (around 100 °C) has been re-injected continuously for over 10 yr. However, differences are present when looking at the small-scale resistivity variations due to the different data coverage and sensitivity of the ERT and TEM methods. Interestingly, the strong conductive anomaly lies mainly in-between TEM soundings but is none the less retrieved by the 3-D inversion consistently with 2-D ERT inversion.

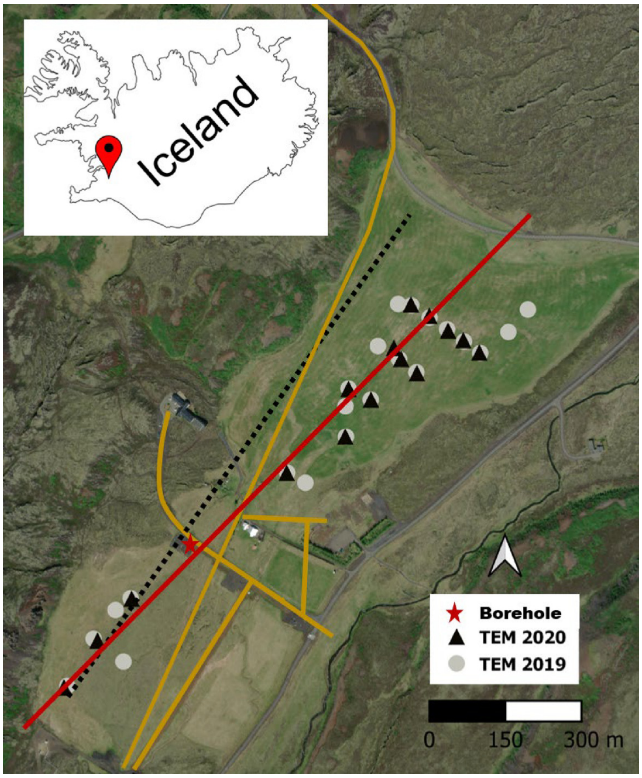

Figure 6. Map of Nesjavellir field site with measurement locations. Grey circles, black triangles and the red star represent the 2019, 2020 TEM and borehole locations, respectively. The dashed line indicates the location of an ERT profile acquired in 2020 and used for comparison. The solid red line represents the position of the profile along which the inversion results are shown. The solid yellow lines indicate the power plant infrastructures at the site.

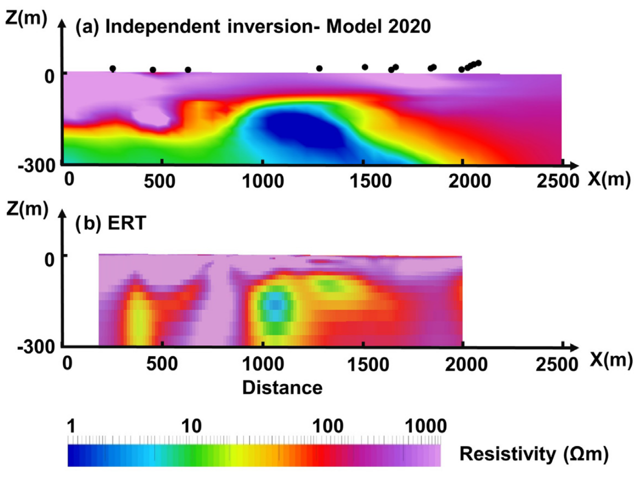

Figure 7. SW-NE profiles of 2020 3-D TEM inversion and 2-D ERT inversion along the black dashed line in Fig. 6, where the data sets were both collected in 2020. Black dots on the top sections represent the TEM sounding positions' projection.

As shown in the synthetic example, the TL inversion results are affected by choice of the MS tuning setting α (eq. 13), especially with coarse data coverage. Figs 8 and 9 present the variation of data misfit as a function of α (as overall variation and sounding by sounding, respectively). At the same time, Figs 10 and 11 show the inversion models in comparison with independent inversions (along with the red profile of Fig. 6 or in 3-D view, respectively).

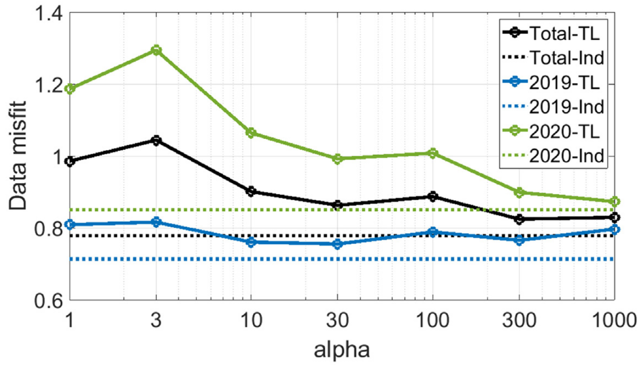

Figure 8. The data misfit of the independent (Ind, dashed lines) and TL (solid lines) inversions for 2019 data (blue lines), 2020 data (green lines) and total data (black lines) as a function of α values (eq. 13).

Fig. 8 tells us that the inversion of the 2019 data set is weakly influenced by the weight of the TL constraints in the objective function (i.e. by α), while a significant influence appears on the 2020 data: with increasing α, two significant drops in data misfit present at $\alpha = 10$ and 300. Fig. 9 presents the data misfit differentiated by sounding and magnetic dipole moment for three α-values. It highlights that the changes in data misfit occur in the 2020 high-moment data in the vicinity of the conductive anomaly and the 2020 low-moment data in the northeast part of the survey. Again, the 2020 high-moment data in the vicinity of the anomaly are the data most affected by the inductive coupling at the site, with some soundings culled before inversion. Ideally, all coupled data have been culled. Still, with a sparse data set, unique identification of coupled data is challenging, and there might be small coupling effects remaining in some of these soundings. This means that the misfit changes might be due to not entirely removed coupling.

Fig. 10 presents the sections of the 2019 and 2020 inversion models along the red line of Fig. 6 and the resistivity ratios of the 2020/2019 inversions for both independent inversions and TL inversions at the three different α-values (3, 30 and 300). All the inversion results present similar resistivity patterns, with the highly conductive body also shown in Fig. 7 lying mostly in the gap of TEM measurements (between 800 and 1200 m along the profile). Nonetheless, slight differences in the shape of the conductive region and the entire resistivity pattern exist among inversions obtained with different settings. The resistivity ratio plots of Fig. 10 help significantly in quantifying the temporal changes over the two models: very few variations exist between the 2019 and 2020 models with the $\alpha = 3$ and 30 TL inversions, while the $\alpha = 300$ TL inversion presents more differences, but always significantly more focused than independent inversions. This is even more evident in Fig. 11, which presents the inversion ratio images in 3-D view within two ratio thresholds: from $-\infty$ to 0.8 for highlighting significant resistivity reductions; from 1.25 to ∞ for highlighting significant resistivity increases. As in Fig. 10, the TL inversions with $\alpha = 3$ and 30 present almost no variation, and the larger α results in more changes in the inversion. However, in Fig. 11, it is shown more clearly than in Fig. 10 that the independent inversions present massive changes over the entire inversion volume, especially when looking at the resistivity increases in Fig. 11(h).

Looking at all inversion results obtained by tuning the α setting, that is, the weight of the TL constraints in the objective function helps in the interpretation: increasing α, more and more variations in

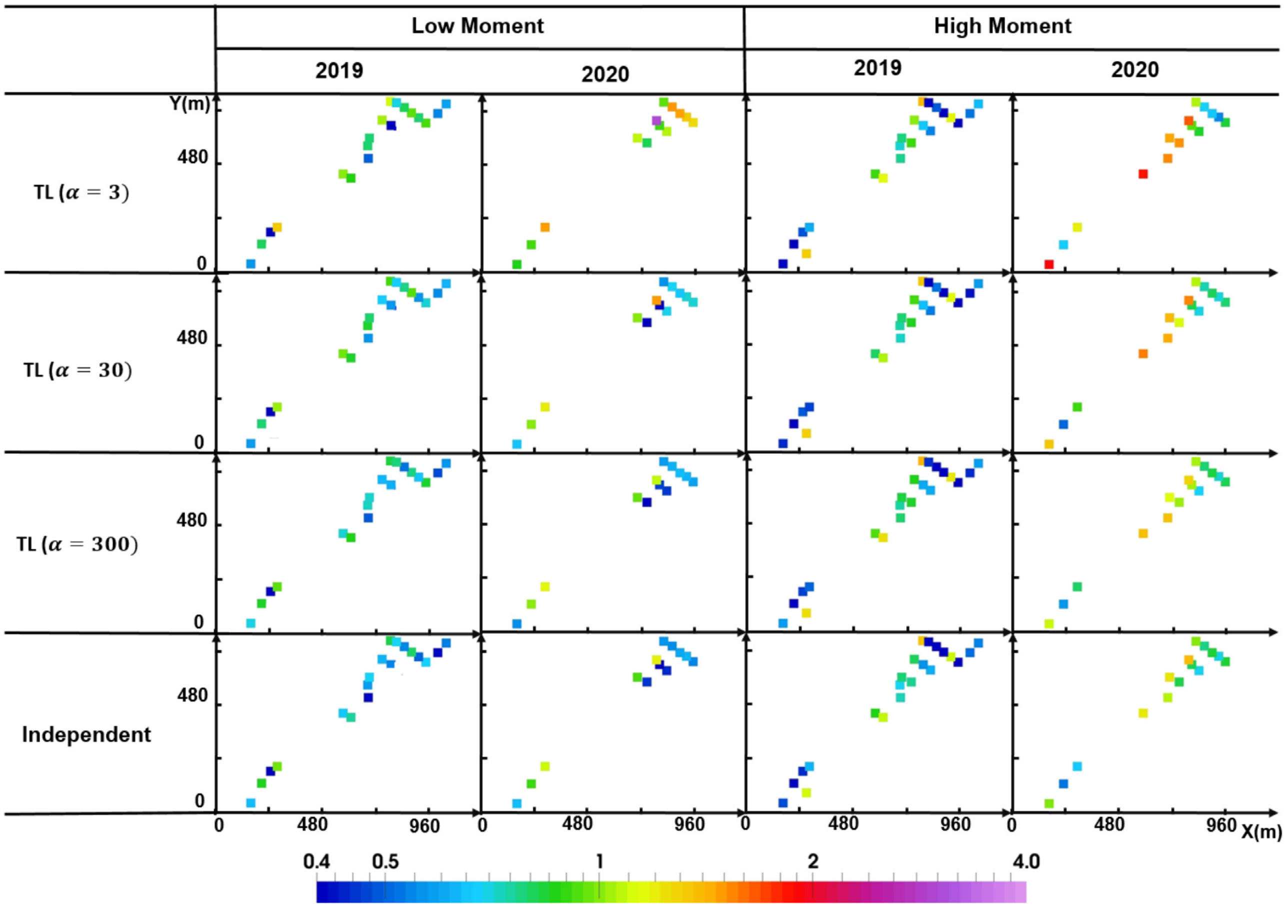

Figure 9. Map of data misfit at individual soundings of TL inversions with different α-values (eq. 13) and independent inversions, separate for moments (low and high) and acquisition years (2019 and 2020).

TL inversion are allowed. So, starting from small α-values, the most data-driven TL changes start to appear, whilst bigger TL changes occur when releasing α, together with an increase in volume of the anomalies already present with small α-values. Consequently, the most data-driven TL changes are the shallow resistivity increases in the northeast area of the survey and the resistivity increase in the southwest area at around 150 m depth (around 1800 and 300 m in Figs 10i and j with $\alpha = 3$ and 30 results). Unfortunately, no prior or borehole information exists that can help interpret these anomalies, which appear data-driven.

Further TL changes appear in new areas of the survey, close to the gap between TEM soundings, only with $\alpha = 300$: with this setting, a reduction in resistivity appears at intermediate-large depths in the 2020 model. This corresponds to a slight decrease in the data misfit in the TEM soundings in the northeast side of the gap, as shown in Fig. 9. Unfortunately, as already stated, this area of the survey is the one most affected by inductive coupling (this is actually the reason for the data gap), so a slight decrease in the data fit is not necessarily significant, considering that there is a risk of coupling contamination in the data. Furthermore, the synthetic experiments have shown that inversion artefacts appear with high α-values, and that the TL changes that occur in acquisition areas with low sounding coverage might be misplaced.

Consequently, even if it is not possible to define unequivocally, only by TEM data and prior information, if a resistivity decrease occurred in the conductive anomaly, that is, if the TL inversion with $\alpha = 300$ has to be preferred to the TL inversion with $\alpha = 30$, at this stage of the research the no-variation scenario is preferred. This outcome would have been much more difficult to conclude based on the independent inversions alone. Furthermore, the TL inversion proposed in this study easily allows to handle a data set with different acquisition layouts and to study the data influence on the inversion results in detail, considerably increasing the robustness of the interpretation.

DISCUSSION

This study presents a new TL inversion scheme for TEM data based on a multimesh approach for model definition and forward computations, 3-D sensitivity calculation during the inversion, and simultaneous inversion of two data sets at once, imposing TL constraints defined in terms of a generalized MS norm, which ensures compact TL changes. The presented synthetic and field examples highlight the capability of the new inversion scheme in handling data repetition with a non-coincident acquisition layout and the capability of retrieving localized TL changes thanks to the 3-D forward and Jacobian implementation also when the non-optimal data coverage is used.

However, especially when it comes to the interpretation of field results, the importance of the regularization of the inversion results appears. This is because, contrary to the synthetic examples in which results can be evaluated based on the knowledge of the

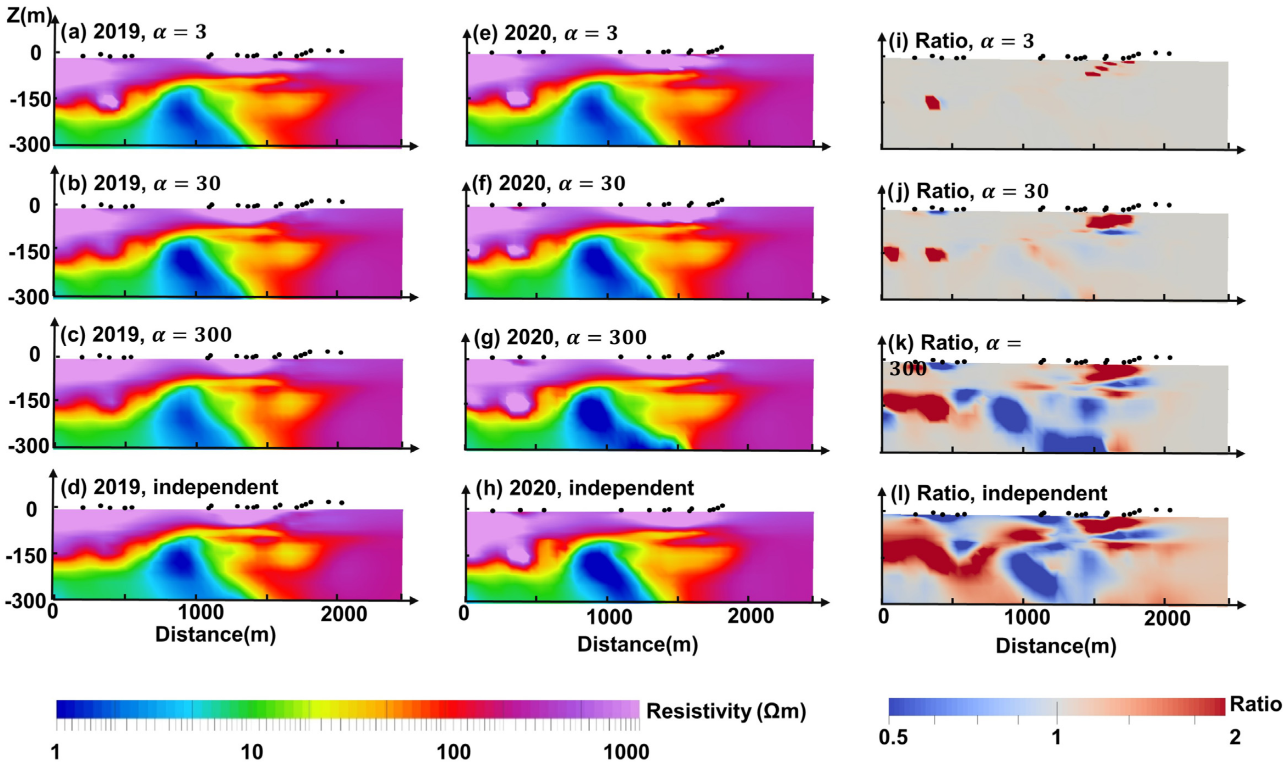

Figure 10. SW-NE inversion model sections for 2019 data (left-hand column) and 2020 data (middle column), as well as 2020/2019 resistivity ratios (right-hand column). Rows from top to bottom show TL inversions with increasing α values (eq. 13) and independent inversions. Black dots on the top sections represent the TEM sounding positions' projection.

true models, the field experiments usually bear much less ground-truthing information to judge the quality of the inversion models. In this study, to draw our conclusions on the interpretation without any direct borehole information, we focused on the analysis of the data misfit and the analysis of the balance between data and model regularization in the objective function, as well on the comparison with the synthetic results. The examples are shown in this manuscript focus, for brevity, on the tuning of the MS setting α, which determines the balance of data misfit and TL regularization in the inversion. However, the tuning of the spatial smoothness of the inversion models and the other settings of the generalized asymmetric MS norm also determine the inversion models and play a significant role in the interpretation, so great care is recommended in the choice of all regularization settings for TL inversions. Furthermore, in many TL experiments diffusive processes are monitored, and compact TL changes do not necessarily represent the underlying physics/geochemistry. The new TL inversion scheme for TEM data is applicable also with classic L2 TL regularization; none the less, regularizations that favour the smallest model variation compatible with the data can be a very helpful tool for data interpretation also when studying diffusive processes, when used together with model measures that promote smooth variations.

CONCLUSIONS

We have developed a new algorithm to carry out TL inversion of TEM data with three features designed for improving applicability and robustness, that is, (1) a 3-D octree-based forward and sensitivity computation, which allows the algorithm to be also applied when the sounding distances in the acquisition layout are more significant than the horizontal extension of background resistivity variations and TL changes; (2) a multimesh approach for forward and inversion computations, such that the same inversion mesh is applicable even in the presence of variations in the acquisition layouts and (3) a focusing of TL changes by the use of the asymmetric MS norm.

We tested the new algorithm on both synthetic and field data. The synthetic experiments modelled a growing 3-D conductive anomaly hosted in a two-layer resistive background, captured by two sets of measurements with slight variations in the sounding positions. Furthermore, two acquisition layouts were modelled: a dense one, with sounding spacing closer than the horizontal extension of the anomaly, and a coarse one, in which the sounding spacing exceeded the anomaly extension. The results show that excellent recovery of TL changes can be achieved with dense data coverage, and that with coarse, non-optimal acquisition density, it is possible to identify the occurrence of resistivity variations, but with misplacement of TL changes. In all cases, the presented approach delivers much more focused changes with clear background, compared to independent inversions.

In the field example, we used two TEM data sets collected in 2019 and 2020 at the Nesjavellir power plant in Southwest Iceland within the GEMGAS project, to establish a baseline for monitoring an experiment of H_2S sequestration, which started in 2021. Due to the coupling from local infrastructures, only very few soundings

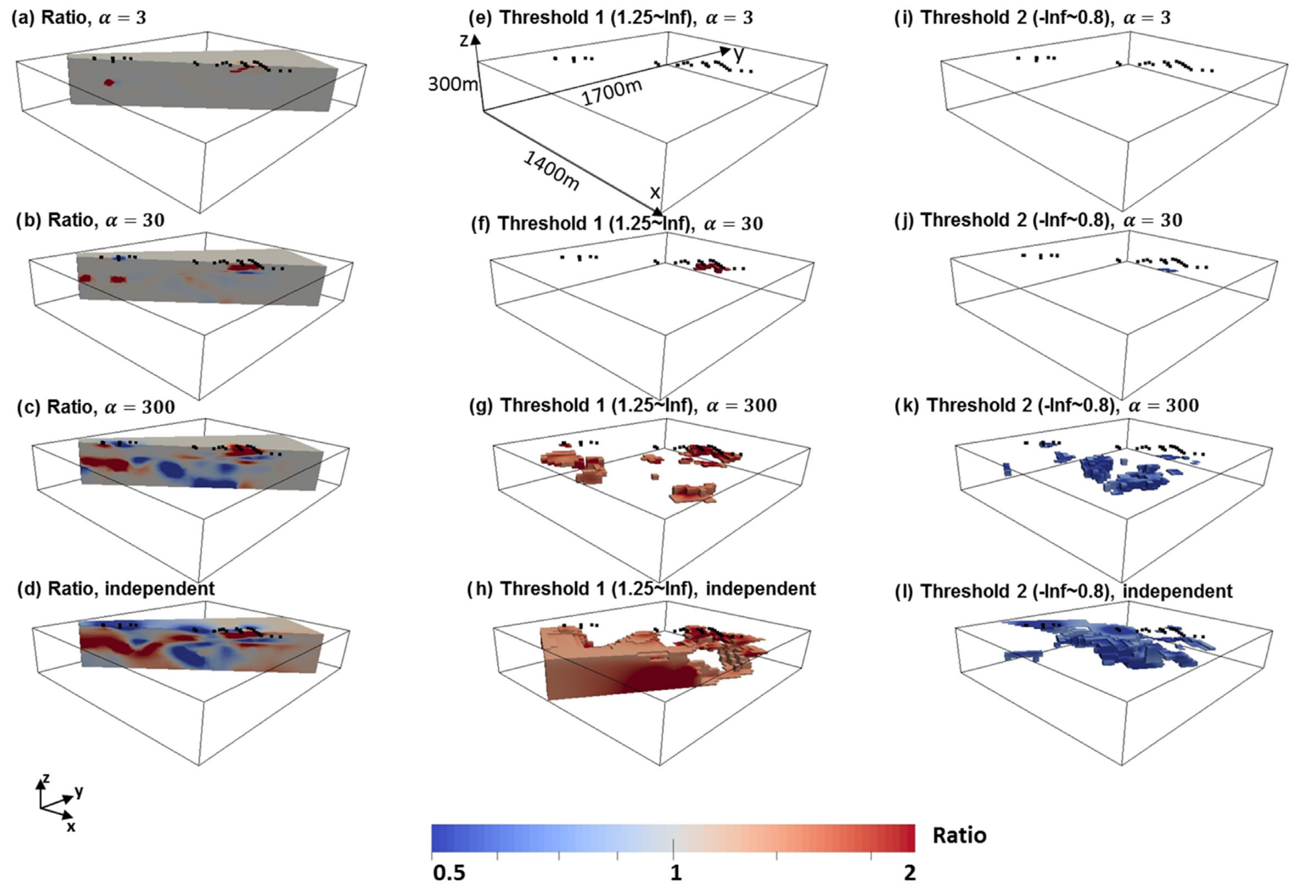

Figure 11. The resistivity ratio and ratio volume within two thresholds $-\infty$-0.8 and 1.25-∞) of TL inversions with different α value and the independent inversion.

close to the injection area could be used. However, the 3-D sensitivity of the new TL algorithm allowed reasonably clear imaging of the subsurface resistivity distribution over the whole domain, as confirmed by the comparison of the inversion models of the TEM data and of the ERT data acquired at the site in 2020 within GEMGAS.

The TL inversions of field data were carried out by varying the weight of the TL constraints (i.e. α-value) on the inversion objective function to better interpret the role of the regularization in the interpretation and specifically of focusing effect of the asymmetric MS norm. All inversions carried out with the new TL algorithm gave much more focused TL changes when compared to independent inversions. Furthermore, the various values used in tuning the asymmetric MS norm identified the likely data-driven model changes between 2019 and 2020.

This new implementation will help in increasing the applicability of TEM method in TL monitoring also in applications in which the presence of infrastructures limits data coverage and the sounding location cannot be repeated exactly.

ACKNOWLEDGMENTS

This project was funded by the Icelandic Centre for Research (Rannis), grant no. 198637-0611. We thank Dr Paul McLachlan for the language polishing. We genuinely appreciate Dr Daniel Blatter, an anonymous reviewer, Editor Dr Ute Weckmann and Asisstant Editor Dr Fern Storey for generously giving their time and constructive comments to make the paper more complete.

DATA AVAILABILITY

Data can be made available by contacting the corresponding author. The TL inversion code has been implemented in the existing inversion software AarhusInv (hgg.au.dk), which is free for academic use.

REFERENCES

Ajo-Franklin, J., Minsley, B. & Daley, T., 2007. Applying compactness constraints to differential traveltime tomography, *Geophysics,* **72,** R67–R75.

Auken, E., Boesen, T. & Christiansen, A.V., 2017. A review of airborne electromagnetic methods with focus on geotechnical and hydrological applications from 2007 to 2017, *Adv. Geophys.,* **58,** 47–93.

Auken, E., *et al.* 2015. An overview of a highly versatile forward and stable inverse algorithm for airborne, ground-based and borehole electromagnetic and electric data, *Explor. Geophys.,* **2015,** 223–235.

Auken, E., Doetsch, J., Fiandaca, G., Christiansen, A.V., Gazoty, A., Cahill, A.G. & Jakobsen, R., 2014. Imaging subsurface migration of dissolved CO2 in a shallow aquifer using 3-D time-lapse electrical resistivity tomography, *J. appl. Geophys.*, 31–41.

Auken, E., Foged, N., Larsen, J.J., Lassen, K.V.T., Maurya, P.K., Dath, S.M. & Eiskjær, T.T., 2019. tTEM—a towed transient electromagnetic system for detailed 3D imaging of the top 70 m of the subsurface, *Geophysics,* **84,** E13–E22.

Bièvre, G., Jongmans, D., Lebourg, T. & Carrière, S., 2021. Electrical resistivity monitoring of an earthslide with electrodes located outside the unstable zone (Pont-Bourquin landslide, Swiss Alps), *Near Surf. Geophys.,* **19,** 225–239.

Blanchy, G., *et al.* 2020. Time-lapse geophysical assessment of agricultural practices on soil moisture dynamics, *Vadose Zone J.,* **19,** e20080, doi.org/10.1002/vzj2.20080.

Bretaudeau, F., Dubois, F., Kassa, S.-G.B., Coppo, N., Wawrzyniak, P. & Darnet, M., 2021. Time-lapse resistivity imaging : CSEM-data 3D double-difference inversion and application to the Reykjanes geothermal field, *Geophys. J. Int,* doi.org/10.1093/gji/ggab172.

Butcher, J.C. & Goodwin, N., 2008. *Numerical Methods for Ordinary Differential Equations,* Vol. **2,** Wiley Online Library.

Carbajal, M.R., Linde, N. & Kalscheuer, T., 2012. Focused time-lapse inversion of radio and audio magnetotelluric data, *J. appl. Geophys.,* **84,** 29–38.

Christensen, N.K., Ferre, T.P.A., Fiandaca, G. & Christensen, S., 2017. Voxel inversion of airborne electromagnetic data for improved groundwater model construction and prediction accuracy, *Hydrol. Earth Syst. Sci.,* **21,** 1321–1337.

Daily, W., Ramirez, A., LaBrecque, D. & Nitao, J., 1992. Electrical resistivity tomography of vadose water movement, *Water Resour. Res.,* **28,** 1429–1442.

Doetsch, J., Fiandaca, G., Auken, E., Christiansen, A.V., Cahill, A.G. & Jakobsen, R., 2015. Field-scale time-domain spectral induced polarization monitoring of geochemical changes induced by injected CO2 in a shallow aquifer, *Geophysics,* **80,** WA113–WA126.

Doetsch, J., Linde, N., Vogt, T., Binley, A. & Green, A.G., 2012. Imaging and quantifying salt-tracer transport in a riparian groundwater system by means of 3D ERT monitoring, *Geophysics,* **77,** B207–B218.

Falgàs, E., Ledo, J., Marcuello, A. & Queralt, P., 2009. Monitoring freshwater-seawater interface dynamics with audiomagnetotelluric data, *Near Surf. Geophys.,* **7,** 391–400.

Farquharson, C.G. & Oldenburg, D.W., 1998. Non-linear inversion using general measures of data misfit and model structure, *Geophys. J. Int.,* **134,** 213–227.

Farzamian, M., Autovino, D., Basile, A., De Mascellis, R., Dragonetti, G., Monteiro Santos, F., Binley, A. & Coppola, A., 2021. Assessing the dynamics of soil salinity with time-lapse inversion of electromagnetic data guided by hydrological modelling, *Hydrol. Earth Syst. Sci.,* **25,** 1509–1527.

Fiandaca, G., Doetsch, J., Vignoli, G. & Auken, E., 2015. Generalized focusing of time-lapse changes with applications to direct current and time-domain induced polarization inversions, *Geophys. J. Int.,* **203,** 1101–1112.

Hanke, M., 1997. A regularizing Levenberg-Marquardt scheme, with applications to inverse groundwater filtration problems, *Inverse Prob.,* **13,** 79.

Hayley, K., Pidlisecky, A. & Bentley, L., 2011. Simultaneous time-lapse electrical resistivity inversion, *J. appl. Geophys.,* **75,** 401–411.

Hermans, T., Wildemeersch, S., Jamin, P., Orban, P., Brouyère, S., Dassargues, A. & Nguyen, F., 2015. Quantitative temperature monitoring of a heat tracing experiment using cross-borehole ERT, *Geothermics,* **53,** 14–26.

Hoversten, G.M. & Schwarzbach, C., 2021. Monitoring hydraulic fracture volume using borehole to surface electromagnetic and conductive proppant, *Geophysics,* **86,** E93–E109.

Jin, J.-M., 2015. *The Finite Element Method in Electromagnetics,* John Wiley & Sons.

Karaoulis, M., Tsourlos, P., Kim, J.-H. & Revil, A., 2014. 4D time-lapse ERT inversion: introducing combined time and space constraints, *Near Surf. Geophys.,* **12,** 25–34.

Kim, J.-H., Yi, M.-J., Park, S.-G. & Kim, J.G., 2009. 4-D inversion of DC resistivity monitoring data acquired over a dynamically changing earth model, *J. appl. Geophys.,* **68,** 522–532.

Kim, K.-J. & Cho, I.-K., 2011. Time-lapse inversion of 2D resistivity monitoring data with a spatially varying cross-model constraint, *J. appl. Geophys.,* **74,** 114–122.

LaBrecque, D.J. & Yang, X., 2001. Difference inversion of ERT data: a fast inversion method for 3-D in situ monitoring, *J. Environ. Eng. Geophys.,* **6,** 83–89.

Last, B. & Kubik, K., 1983. Compact gravity inversion, *Geophysics,* **48,** 713–721.

Lesparre, N., Nguyen, F., Kemna, A., Robert, T., Hermans, T., Daoudi, M. & Flores-Orozco, A., 2017. A new approach for time-lapse data weighting in electrical resistivity tomography, *Geophysics,* **82,** E325–E333.

Lévy, L., Gibert, B., Sigmundsson, F., Flóvenz, Ó.G., Hersir, G.P., Briole, P. & Pezard, P.A., 2018. The role of smectites in the electrical conductivity of active hydrothermal systems: electrical properties of core samples from Krafla volcano, Iceland, *Geophys. J. Int.,* **215,** 1558–1582.

Lévy, L., Gibert, B., Sigmundsson, F., Parat, F., Deldicque, D. & Hersir, G.P., 2019. Tracking magmatic hydrogen sulphur circulations using electrical impedance : complex electrical properties of core samples at the Krafla volcano, Iceland, *J. geophys. Res.: Solid Earth,* 124, doi.org/10.1029/2018JB016814.

Lévy, L., *et al.* 2020. Geo-electrical monitoring of H2S mineralization into pyrite, upon re-injection in basalts at Nesjavellir Geothermal site, Iceland, in *World Geothermal Congress 2020+1,* Reykjavik, Iceland.

Madsen, L.M., Fiandaca, G. & Auken, E., 2020. 3-D time-domain spectral inversion of resistivity and full-decay induced polarization data—full solution of Poisson's equation and modelling of the current waveform, *Geophys. J. Int.,* **223,** 2101–2116.

McLachlan, P., Chambers, J., Uhlemann, S. & Binley, A., 2017. Geophysical characterisation of the groundwater–surface water interface, *Adv. Water Res.,* **109,** 302–319.

McLachlan, P., Chambers, J., Uhlemann, S., Sorensen, J. & Binley, A., 2020. Electrical resistivity monitoring of river–groundwater interactions in a Chalk river and neighbouring riparian zone. *Near Surf. Geophys.,* **18,** 385–398

Menke, W., 2018. *Geophysical Data Analysis: Discrete Inverse Theory,* Pages, Academic press.

Miller, C.R., Routh, P.S., Brosten, T.R. & McNamara, J.P., 2008. Application of time-lapse ERT imaging to watershed characterization, *Geophysics,* **73,** G7–G17.

Nyboe, N.S., Jørgensen, F. & Sørensen, K., 2010. Integrated inversion of TEM and seismic data facilitated by high penetration depths of a segmented receiver setup, *Near Surf. Geophys.,* **8,** 467–474.

Ogilvy, R., *et al.* 2009. Automated monitoring of coastal aquifers with electrical resistivity tomography, *Near Surf. Geophys.,* **7,** 367–376.

Oldenborger, G.A., Knoll, M.D., Routh, P.S. & LaBrecque, D.J., 2007. Time-lapse ERT monitoring of an injection/withdrawal experiment in a shallow unconfined aquifer, *Geophysics,* **72,** F177–F187.

Orange, A., Key, K. & Constable, S., 2009. The feasibility of reservoir monitoring using time-lapse marine CSEM, *Geophysics,* **74,** F21–F29.

Peacock, J.R., Thiel, S., Heinson, G.S. & Reid, P., 2013. Time-lapse magnetotelluric monitoring of an enhanced geothermal system, *Geophysics,* **78,** B121–B130.

Portniaguine, O. & Zhdanov, M.S., 1999. Focusing geophysical inversion images, *Geophysics,* **64,** 874–887.

Prikryl, J., Marieni, C., Gudbrandsson, S., Aradóttir, E.S., Gunnarsson, I. & Stefánsson, A., 2018. H 2 S sequestration process and sustainability in geothermal systems, *Geothermics,* **71,** 156–166.

Rosas-Carbajal, M., Linde, N., Peacock, J., Zyserman, F.I., Kalscheuer, T. & Thiel, S., 2015. Probabilistic 3-D time-lapse inversion of magnetotelluric data: application to an enhanced geothermal system, *Geophys. Suppl. Mon. Not. Roy. Astron. Soc.,* **203,** 1946–1960.

Shantsev, D.V., Nerland, E.A. & Gelius, L.-J., 2020. Time-lapse CSEM: how important is survey repeatability?, *Geophys. J. Int.,* **223,** 2133–2147.

Singha, K., Day-Lewis, F.D., Johnson, T. & Slater, L.D., 2015. Advances in interpretation of subsurface processes with time-lapse electrical imaging, *Hydrol. Process.,* **29,** 1549–1576.

Vann, S., Puttiwongrak, A., Suteerasak, T. & Koedsin, W., 2020. Delineation of seawater intrusion using geo-electrical survey in a coastal aquifer of Kamala Beach, Phuket, Thailand, *Water,* **12,** 506.

Vignoli, G., Deiana, R. & Cassiani, G., 2012. Focused inversion of vertical radar profile (VRP) traveltime data, *Geophysics,* **77,** H9–H18.

Xiao, L., Fiandaca, G., Zhang, B., Christiansen, A. V. & Auken, E., 2022. Fast 2.5D and 3D Inversion of transient electromagnetic surveys using the octree-based finite element method, *Geophysics,* in print, doi.org/10.1190/geo2021-0402.1.

Yang, D., Oldenburg, D.W. & Haber, E., 2013. 3-D inversion of airborne electromagnetic data parallelized and accelerated by local mesh and adaptive soundings, *Geophys. J. Int.,* **196,** 1492–1507.

Zhang, B., Engebretsen, K.W., Fiandaca, G., Cai, H. & Auken, E., 2021. 3D inversion of time-domain electromagnetic data using finite elements and a triple mesh formulation, *Geophysics,* **86,** E257–E267.

Zhdanov, M. & Tolstaya, E., 2004. Minimum support nonlinear parametrization in the solution of a 3D magnetotelluric inverse problem, *Inverse Probl.,* **20,** 937.

Zhdanov, M., Vignoli, G. & Ueda, T., 2006a. Sharp boundary inversion in crosswell travel-time tomography, *J. geophys. Eng.,* **3,** 122–134.

Zhdanov, M.S., Lee, S.K. & Yoshioka, K., 2006b. Integral equation method for 3D modeling of electromagnetic fields in complex structures with inhomogeneous background conductivity, *Geophysics,* **71,** G333–G345.